HD 66051: the first eclipsing binary hosting an early-type magnetic star

O. Kochukhov, C. Johnston, E. Alecian, G. A. Wade

Monthly Notices
of the
ROYAL ASTRONOMICAL SOCIETY

MNRAS **478,** 1749–1762 (2018)
Advance Access publication 2018 May 02

doi:10.1093/mnras/sty1118

HD 66051: the first eclipsing binary hosting an early-type magnetic star

O. Kochukhov,[1]★ C. Johnston,[2] E. Alecian,[3] G. A. Wade[4] and the BinaMIcS collaboration

[1]*Department of Physics and Astronomy, Uppsala University, Box 516, 751 20 Uppsala, Sweden*
[2]*Instituut voor Sterrenkunde, KU Leuven, Celestijnenlaan 200D, 3001, Leuven, Belgium*
[3]*Université Grenoble Alpes, CNRS, IPAG, F-38000 Grenoble, France*
[4]*Department of Physics and Space Science, Royal Military College of Canada, PO Box 17000, Stn Forces, Kingston, Ontario K7K 7B4, Canada*

Accepted 2018 April 27. Received 2018 April 27; in original form 2018 March 6

ABSTRACT

Early-type magnetic stars are rarely found in close binary systems. No such objects were known in eclipsing binaries prior to this study. Here we investigated the eclipsing, spectroscopic double-lined binary HD 66051, which exhibits out-of-eclipse photometric variations suggestive of surface brightness inhomogeneities typical of early-type magnetic stars. Using a new set of high-resolution spectropolarimetric observations, we discovered a weak magnetic field on the primary and found intrinsic, element-dependent variability in its spectral lines. The magnetic field structure of the primary is dominated by a nearly axisymmetric dipolar component with a polar field strength $B_{\rm d} \approx 600$ G and an inclination with respect to the rotation axis of $\beta_{\rm d} = 13^{\circ}$. A weaker quadrupolar component is also likely to be present. We combined the radial velocity measurements derived from our spectra with archival optical photometry to determine fundamental masses (3.16 and 1.75 $M_{\odot}$) and radii (2.78 and 1.39 $R_{\odot}$) with a 1–3 per cent precision. We also obtained a refined estimate of the effective temperatures (13000 and 9000 K) and studied chemical abundances for both components with the help of disentangled spectra. We demonstrate that the primary component of HD 66051 is a typical late-B magnetic chemically peculiar star with a non-uniform surface chemical abundance distribution. It is not an HgMn-type star as suggested by recent studies. The secondary is a metallic-line star showing neither a strong, global magnetic field nor intrinsic spectral variability. Fundamental parameters provided by our work for this interesting system open unique possibilities for probing interior structure, studying atomic diffusion, and constraining binary star evolution.

Key words: binaries: eclipsing – stars: chemically peculiar – stars: fundamental parameters – stars: individual: HD 66051 (V414 Pup) – stars: magnetic field.

1 INTRODUCTION

The phenomenon of chemical peculiarity is widespread among main sequence B and A stars. Quiescence in the radiative envelopes of these objects facilitates chemical segregation by the competing effects of radiative pressure, gravitational settling, and, occasionally, accretion of ISM material, giving rise to several distinct types of chemically peculiar (CP) stars (see reviews by Smith 1996; Kurtz & Martinez 2000). A significant fraction of these objects (up to ∼ 10 per cent of all OBA stars; Sikora, Wade & Power 2018) possesses prominent, globally organized, kG-strength magnetic fields. These fields, thought to have a fossil origin (Braithwaite & Spruit 2004; Neiner et al. 2015), must have been acquired by stars early in their evolutionary history and remained essentially unchanged in the course of their main sequence life.

The magnetic CP (Ap/Bp) stars are characterized by extreme chemical anomalies and exhibit conspicuous spectral and photometric rotational variability due to inhomogeneous chemical abundance distributions (spots of element over- and underabundance) on their surfaces. On the other hand, the so-called non-magnetic CP stars (cooler Am and hotter HgMn as well as PGa objects) show less extreme abundance peculiarities, little or no surface inhomogeneities and at least two order of magnitude weaker magnetic fields, which likely have a different physical origin than the magnetism of Ap/Bp stars.

It is remarkable that the magnetic and non-magnetic CP stars have drastically different binary characteristics. Whereas the binary

★ E-mail: oleg.kochukhov@physics.uu.se

frequency of Am and HgMn stars is the same or higher than that of normal stars, Ap/Bp stars are almost entirely absent in close binary systems (Gerbaldi, Floquet & Hauck 1985; Carrier et al. 2002). For example, among hundreds of known magnetic BA stars, only about 10 belong to spectroscopic binaries with $P_{\rm orb} < 20$ d (Landstreet et al. 2017) and only one doubly-magnetic early-type binary, ϵ Lup, has been found so far (Shultz et al. 2015).

This unusually low binary incidence of hot magnetic stars suggests that stellar multiplicity is somehow linked with the absence of fossil magnetic fields. Several hypotheses explaining this anticorrelation are discussed in the literature. For instance, numerical simulations of the early massive-star formation stages indicate that the presence of a strong global primordial magnetic field inhibits protostellar cloud fragmentation, disfavouring formation of multiple systems (Commerçon, Hennebelle & Henning 2011). On the other hand, it has been proposed that the field itself originates in the process of pre-main sequence binary star mergers (Schneider et al. 2016). In either case, short-period, early-type, magnetic binary systems are very unusual objects. Despite their low incidence, their sheer existence illuminates uncommon channels of the evolution of massive and intermediate-mass stars. These systems also represent unique astrophysical laboratories which enable us to derive useful constraints on the fundamental parameters of the binary companions. These constraints are particularly valuable considering the peculiar, non-standard structure of the chemically stratified atmospheres and outer envelopes of magnetic CP stars.

HD 66051 (V414 Pup, HIP 39229), $V = 8.8$, is listed as an A0 Si object in the catalogue of CP stars by Renson & Manfroid (2009). Based on the Hipparcos (Perryman et al. 1997) and ASAS-3 (Pojmanski 2002) photometry, Otero (2003) showed the presence of eclipses in the light curve of HD 66051 accompanied by a smooth, stable, synchronous out-of-eclipse variability. This observation suggested that one of the binary components in this system exhibits an intrinsic rotational variability due to surface spots. Further photometric analysis of HD 66051 by Hümmerich, Paunzen & Bernhard (2016) reinforced the conclusions by Otero (2003) and confirmed that the primary component is a late-B chemically peculiar star with enhanced Si II lines. This spectroscopic characteristic is a typical signature of the magnetic Bp stars, raising the intriguing possibility that the primary of HD 66051 is a CP star with a global magnetic field.

Another photometric and spectroscopic study of HD 66051 was carried out by Niemczura et al. (2017, hereafter N17). These authors obtained photometric time series observations in several filters, determined atmospheric parameters of both components, and presented detailed abundance analysis of the primary based on two spectroscopic observations. They argued that the primary of HD 66051 is, in fact, not a magnetic Bp star but an object closely related to HgMn stars. The latter sub-group of late-B CP stars overlaps with the magnetic Bp stars in the H-R diagram but lacks global magnetic fields (Aurière et al. 2010; Kochukhov et al. 2013). Moreover, unlike Bp stars, HgMn stars are commonly found in close binaries (Smith 1996; Schöller et al. 2010; Folsom, Wade & Alecian 2013a), including eclipsing systems (e.g. Folsom et al. 2010). These stars exhibit moderate atmospheric abundance anomalies and weak surface inhomogeneities (Makaganiuk et al. 2011b; Korhonen et al. 2013), typically detectable only with a high signal-to-noise (S/N) ratio, high-resolution spectroscopy (e.g. Adelman et al. 2002; Kochukhov et al. 2005, 2011) or with high-precision space-based photometry (Morel et al. 2014; Strassmeier et al. 2017).

Paunzen et al. (2018) combined the photometric observations of HD 66051 by N17 with 12 radial velocity measurements obtained from high- and medium-resolution spectra. Based on this data set, they derived astrophysical parameters of the system and compared these results with the predictions of stellar evolutionary models.

In this paper we investigate the nature of HD 66051 with the help of new high-resolution, time series spectroscopic and spectropolarimetric observations. We report discovery of a global magnetic field and spectral variability of the primary component, demonstrating it to be a typical magnetic Bp star rather than a HgMn-related object as hypothesized by N17. Furthermore, we combine archival photometry with our new spectroscopic radial velocity (RV) measurements to derive precise fundamental masses and radii for both components of HD 66051. This makes the primary of this system the first magnetic Bp star for which such fundamental constraints have become available.

The rest of our paper is organized as follows. Section 2 discusses the observational material used in our study. Section 3 presents analysis of these data, including investigation of the magnetic field, line profile variability, simultaneous RV and light curve binary star modelling, and assessment of the atmospheric parameters and abundances. The main conclusions of our study are summarized and discussed in Section 4.

2 OBSERVATIONAL DATA

We observed HD 66051 in 2016 December and 2017 January with the ESPaDOnS spectropolarimeter at the Canada-France-Hawaii Telescope (CFHT). These observations were carried out in the framework of the BinaMIcS CFHT large program (Alecian et al. 2015). Fourteen circular polarization observations of HD 66051 were acquired on 13 individual nights. Each polarimetric measurement comprised four subexposures obtained with two different polarimeter configurations in order to exchange the path of the orthogonal polarization beams through the system and their position on the detector. Twelve observations were obtained with a 300 s subexposure time (yielding 1200 s total exposure time); two measurements were obtained with a 840 s subexposure time (3360 s total exposure time).

All spectra were reduced with the LIBRE-ESPRIT software (Donati et al. 1997) running at the telescope. The intensity (Stokes I) spectra were obtained by adding together orthogonal polarization beams from all four subexposures. The circular polarization (Stokes V) spectra were derived using the ratio method (Bagnulo et al. 2009) to minimize systematic errors due to instrumental artefacts. The same four subexposures were also used to obtain a diagnostic null spectrum in order to assess residual systematic errors. Continuum normalization was performed by iteratively fitting a smooth function to the upper envelope of the merged stellar spectrum (Rosén et al. 2018), excluding telluric and hydrogen line regions. The resulting spectra have a resolving power of 65000 and provide a nearly complete coverage of the 3700–10480 Å wavelength range. The S/N ratio varies from 200 to 370 and has a median value of 250.

The complete log of our spectropolarimetric observations of HD 66051 is presented in Table 1. Columns 1–4 give the UT date of observation, the heliocentric Julian date corresponding to the middle of observation, the orbital phase, and the median S/N ratio per 1.8 km s^{-1} velocity bin in the 5000–6000 Å wavelength region. The orbital phase was calculated according to the ephemeris HJD = 2452167.8724+ $E \times 4.7492148$ determined in Section 3.3. The same ephemeris gives the rotational phase of the primary (the

Table 1. Journal of spectropolarimetric observations of HD 66051. The columns indicate the date of observation, Heliocentric Julian Date at the middle of the observing sequence, orbital phase, median S/N ratio of the spectra in the 5000–6000 Å wavelength interval, S/N of LSD profiles, radial velocities of the primary and secondary, mean longitudinal magnetic field of the primary, false alarm probability for the Stokes *V* signature of the primary, and the corresponding field detection significance (ND=no detection, DD=definite detection).

UT date	HJD	Phase	S/N_{obs}	S/N_{LSD}	V_1 (km s^{-1})	V_2 (km s^{-1})	$\langle B_z \rangle$ (G)	FAP	Detection
2016-12-15	2457737.9971	0.852	253	10661	59.8	−113.5	32 ± 26	0.0	DD
2016-12-21	2457744.0766	0.132	241	10364	−57.2	99.9	54 ± 27	5.1×10^{-1}	ND
2016-12-22	2457744.9862	0.323	261	11278	−71.3	120.0	1 ± 26	7.4×10^{-1}	ND
2017-01-08	2457761.9942	0.905	225	9741	41.6	−79.7	10 ± 28	0.0	DD
2017-01-09	2457763.0279	0.122	257	11037	−54.1	94.9	23 ± 25	1.5×10^{-1}	ND
2017-01-10	2457764.0415	0.336	256	11176	−68.4	116.5	−5 ± 26	1.1×10^{-1}	ND
2017-01-11	2457765.0367	0.545	233	9934	19.4	−40.6	10 ± 29	7.9×10^{-1}	ND
2017-01-12	2457766.0215	0.753	250	10884	75.3	−138.7	−39 ± 26	2.9×10^{-12}	DD
2017-01-13	2457767.0361	0.966	270	11782	14.8	−32.1	98 ± 23	0.0	DD
2017-01-14	2457767.9954	0.168	247	10566	−66.9	115.9	24 ± 27	8.0×10^{-1}	ND
2017-01-15	2457769.0496	0.390	241	10321	−52.7	87.0	37 ± 29	1.3×10^{-3}	ND
2017-01-16	2457770.0308	0.597	205	8648	41.3	−80.4	−33 ± 32	9.8×10^{-1}	ND
2017-01-17	2457771.0382	0.809	372	15559	69.7	−132.0	−42 ± 18	0.0	DD
2017-01-17	2457771.0790	0.817	314	13033	68.1	−130.1	−31 ± 21	0.0	DD

hotter, more massive, and more luminous component) since, as confirmed later in the paper, its rotation is synchronized with the orbital motion.

In addition to the ESPaDOnS high-resolution spectropolarimetric observations, we made use of the *B*, *V*, and I_c time series photometry published by N17. We refer the reader to that paper for details of the acquisition and reduction of the photometric data. In addition, we made use of the *V*-band photometric observations from the ASAS-3 project (Pojmanski 2002).

3 ANALYSIS

3.1 Least-squares deconvolved profiles

3.1.1 Calculation of LSD profiles

No circular polarization signal is evident in individual metal lines in any of our Stokes *V* spectra of HD 66051. To enhance the S/N of the polarization profiles and to derive average Stokes *I* spectra amenable to straightforward RV measurements, we employed the least-squares deconvolution (LSD) code developed by Kochukhov, Makaganiuk & Piskunov (2010). This software performs an intelligent co-addition of information from all usable metal lines following the principles described by Donati et al. (1997). In this widely used method, each intensity or polarization spectral feature is assumed to be a shifted and scaled copy of a mean profile. It is also assumed that contributions of overlapping lines add up linearly. The line scaling factors, or weights, are given by the theoretical line depth for Stokes *I* and by the product of the line depth, central wavelength and the effective Landé factor for Stokes *V*. Provided a list of spectral line positions and weights (a line mask) corresponding to a specified set of stellar atmospheric parameters, the LSD algorithm allows one to quickly derive a high S/N ratio mean profile for a given observed spectrum and its error bars. Kochukhov et al. (2010) showed that approximations inherent to the LSD technique are appropriate for a Stokes *I* and *V* profile analysis if the local magnetic field strength does not exceed ∼ 2 kG.

We used the VALD data base (Ryabchikova et al. 2015) to retrieve a line list for $T_{\rm eff} = 12500$ K, $\log g = 4.0$, and element abundances of HD 66051 A as reported by N17. The lines with intrinsic depth less than 10 per cent as well as lines located in the broad hydrogen line wings and in regions contaminated by the telluric absorption were removed. The final LSD line mask included 2359 lines, dominated by Fe II, with the mean wavelength $\lambda_0 = 5160$ Å and mean effective Landé factor $z_0 = 1.18$. The same λ_0 and z_0 were used for the normalization of the LSD profiles.

The LSD procedure was applied to all Stokes *I*, *V*, and diagnostic null spectra. The mean profiles were calculated in the ±350 km s^{-1} velocity range, using a 2 km s^{-1} velocity bin. The resulting S/N ratio of the LSD profiles, reported in the fifth column of Table 1, indicates a factor of ≈ 40 gain with respect to the S/N ratio of the original spectra.

3.1.2 Radial velocity measurements

The Stokes *I* LSD profiles obtained using the line-addition procedure outlined above are displayed in the left-hand panel of Fig. 1. The prominent, slightly variable, absorption signature of the primary component is accompanied by a much weaker contribution of the secondary. The latter appears to be constant in shape and is found to be red-shifted with respect to the primary's profile for phases 0.122–0.390 and blue-shifted for phases 0.545–0.966, in full agreement with the relative radial velocities expected for a circular orbital motion.

A simple mean profile disentangling (component separation) procedure adapted from the method used by Folsom et al. (2010, 2013b) was applied to measure RVs of the HD 66051 components from the Stokes *I* LSD profiles. This version of the disentangling algorithm determines individual, time-dependent radial velocities and mean component profiles under the assumption that the latter are constant in time. This approximation is not strictly correct for HD 66051 A. Nevertheless, in our experience this method yields considerably more robust and accurate radial velocities when applied to stars with spectra moderately distorted by surface spots compared to measurements using the centre-of-gravity method or analytical function fitting (Rosén et al. 2018).

The radial velocities of HD 66051 A and B determined with the help of the LSD profile disentangling technique are given in columns 6 and 7 of Table 1. No realistic error estimate is possible with our disentangling algorithm. But subsequent fitting of the orbital

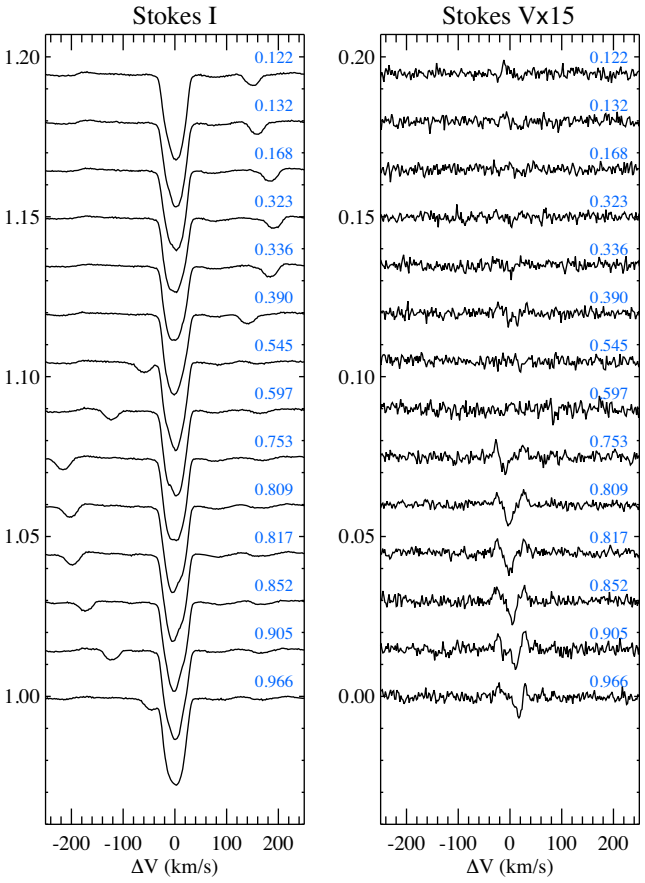

Figure 1. Least-squares deconvolved Stokes *I* (left-hand panel) and Stokes *V* (right-hand panel) profiles of HD 66051. The spectra are shifted to the laboratory frame of the primary component and offset vertically according to the orbital phase indicated next to each profile. The Stokes *V* profiles are amplified by a factor of 15.

solution to these RV data suggests a typical error of 0.7 km s^{-1} for the primary and 1.3 km s^{-1} for the secondary.

3.1.3 Polarization signature detection

Using the radial velocities of the binary components derived from the Stokes *I* LSD profiles, we examined the Stokes *V* LSD spectra in the laboratory frame of the primary component (see the right-hand panel of Fig. 1). This analysis reveals clear polarization signatures at the radial velocity of the primary between orbital phases 0.753 and 0.966. These signatures have no counterparts in the LSD profiles obtained from the diagnostic null spectrum. At the same time, no evidence of a magnetic signature is found at the position of the secondary component. Consequently, these results represent an unambiguous detection of the global magnetic field in HD 66051 A and no detection of magnetic field in HD 66051 B.

Application of the formal false alarm χ^2 probability (FAP) analysis (Donati, Semel & Rees 1992; Donati et al. 1997) to the $\pm$40 km s^{-1} velocity interval around the position of the primary yields a definite magnetic field detection (FAP $< 10^{-5}$) for six Stokes *V* profiles and a non-detection (FAP $> 10^{-3}$) for the remaining eight profiles. Individual FAP values are given in the ninth column of Table 1. Identical analysis applied to the null LSD profiles yields only non-detections, with FAP $\geq 8.4 \times 10^{-1}$.

3.2 Magnetic field strength and topology

3.2.1 Longitudinal magnetic field

To obtain quantitative information about the strength and topology of the global magnetic field of HD 66051 A, we measured the mean longitudinal magnetic field, $\langle B_z \rangle$, from the Stokes *V* LSD profiles. The Stokes *I* signature of the secondary was subtracted prior to these measurements. The mean longitudinal field, which provides a measure of the disc-averaged line-of-sight magnetic field component, was obtained by computing the first moment of the Stokes *V* profile and normalizing it by the equivalent width of the Stokes *I* profile (e.g. Kochukhov et al. 2010)

$$\langle B_z \rangle = -7.145 \times 10^6 \frac{\int (v - v_0) V \mathrm{d}v}{\lambda_0 z_0 \int (1 - I) \mathrm{d}v}, \quad (1)$$

where the velocity coordinate v and the centre-of-gravity velocity of the *I* profile, v_0, are measured in km s^{-1} and the result is in gauss. Owing to the normalization of the Stokes *V* moment by the equivalent width of the intensity profile, $\langle B_z \rangle$ calculated with this formula is unaffected by continuum contribution of a binary companion or any other continuum light source.

We evaluated the integrals in equation (1) with the help of the trapezoidal integration scheme, within $\pm$40 km s^{-1} of the centre-of-gravity of the primary line. The $\langle B_z \rangle$ error was deduced following the standard error propagation rules. The resulting longitudinal field measurements are reported in the eighth column of Table 1. The measured $\langle B_z \rangle$ values span from about $-$40 G to 100 G. The median error is 26 G, which is comparable to $\langle B_z \rangle$ values themselves. In fact, only one longitudinal field measurement at phase 0.966 corresponds to a $>3\sigma$ $\langle B_z \rangle$ detection. This is because several observed Stokes *V* profiles show nearly symmetric polarization signatures. In this case, longitudinal field measurements do not allow one to confidently ascertain the presence of a magnetic field (notwithstanding that the Stokes *V* profiles firmly indicate that a field is present).

The same longitudinal field measurement procedure was applied to the diagnostic null LSD profiles. No formal $\langle B_z \rangle$ detections were obtained, with the most significant $\langle B_z \rangle$(N) value being about 1.6σ. The standard deviation of the 14 $\langle B_z \rangle$(N) values is 21 G, in good agreement with the typical formal error of the Stokes *V* $\langle B_z \rangle$ measurements inferred above.

The mean longitudinal magnetic field of HD 66051 A is illustrated as a function of phase in Fig. 2. Despite the lack of individual $\langle B_z \rangle$ detections, the longitudinal field appears to follow a coherent phase variation. In particular, the minimum around phase 0.7 is well-defined. By fitting this variation with a sinusoid function (solid curve in Fig. 2), we found a constant term $B_0 = 4.7$ G and a semi-amplitude of $B_1 = 43$ G. This fit may be considered unsatisfactory given its reduced chi-square value (χ^2_ν) of 1.9. Adding the first harmonic results in a much better description of the observed $\langle B_z \rangle$ variation (dashed line in Fig. 2). This fit yields χ^2_ν of 0.7, probably indicating overfitting of the data.

To summarize, this analysis of the longitudinal magnetic field of HD 66051 A does not offer much insight into the field characteristics apart from suggesting that the polar field intensity is on the order of a few hundred G and that the field topology is likely not purely dipolar.

3.2.2 Stokes V *profile modelling*

Direct modelling of the LSD Stokes *V* profile signatures offers an alternative approach to obtaining quantitative characteristics of

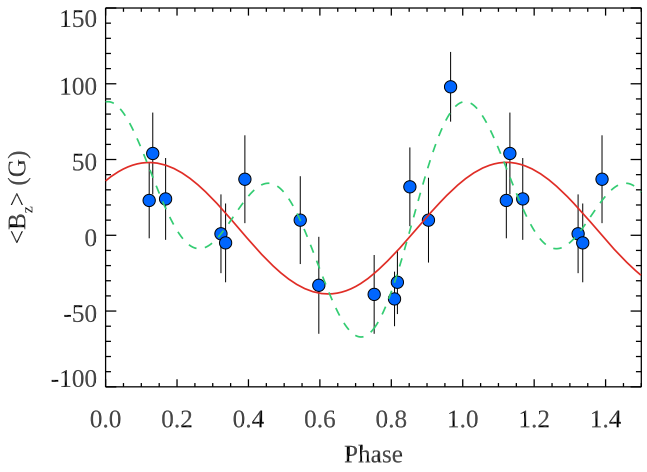

Figure 2. Mean longitudinal magnetic field of the primary component of HD 66051 as a function of rotational phase. The curves illustrate the single-wave (red solid line) and double-wave (green dashed line) Fourier fits.

the global magnetic field of the primary component of HD 66051. Such an analysis is also necessary to address the puzzling phase dependence of the observed Stokes *V* profile amplitude, with only a handful of observations in a limited phase interval showing a definite polarization signature.

The phase coverage and quality of the available LSD profiles is clearly insufficient for a detailed Zeeman Doppler imaging study (e.g. Kochukhov et al. 2014, 2017). Instead, a simpler multipolar fit to the circular polarization data (e.g. Alecian et al. 2008, 2016) can be used to get an idea about the field strength and geometry. In this study we performed such modelling with the help of the GSTOKES code.[1] This tool, written in IDL and equipped with a user-friendly graphical front-end, enables forward calculation of the disc-integrated Stokes parameter profiles as well as magnetic inversions under several widely used simplifying approximations of the polarized line formation. The code implements the Unno–Rachkovsky analytical solution of the polarized radiative transfer equation (e.g. Landi Degl'Innocenti & Landolfi 2004) and the weak-field approximation with the Gaussian local profiles (e.g. Petit & Wade 2012). The magnetic field geometry is described with one of the common low-order multipolar field parametrizations: a centred or offset dipole (Achilleos & Wickramasinghe 1989), a superposition of the aligned, axisymmetric dipole, quadrupole and octupole components (Landstreet 1988), and a dipole plus general, non-axisymmetric quadrupolar field (Bagnulo, Landi degl'Innocenti & Landi degl'Innocenti 1996). Various stellar (line depth, $v_e \sin i$, radial velocity, inclination) and magnetic field parameters can be adjusted for a given set of observed LSD profiles using a powerful non-linear least-squares optimization algorithm (Markwardt 2009).

The present analysis of HD 66051 A was carried out using Gaussian local Stokes *I* profiles with FWHM $= 5\,\mathrm{km\,s^{-1}}$ and calculating the Stokes *V* profiles under the weak-field approximation with $\lambda = 5160$ Å and $z = 1.18$. The linear limb-darkening with a coefficient of 0.37 was also adopted. The stellar rotational axis was assumed to be aligned with the orbital axis. Consequently, the inclination angle of the former was fixed to the value of 86.14° according to the binary system modelling in Section 3.3. In the first step of the analysis the local equivalent width of the intensity profiles, assumed to be constant over the stellar surface, and $v_e \sin i$ were adjusted to reproduce the LSD Stokes *I* spectra. Then, the magnetic field topology was derived from the Stokes *V* spectra.

Initially, we attempted to reproduce the observed Stokes *V* profiles with a centred dipolar field. This analysis yields a polar field strength of $B_d = 472 \pm 111$ G and magnetic obliquity of $\beta_d = 18 \pm 4°$. However, the corresponding fit (dashed line in Fig. 3) to the observed LSD profiles is not entirely satisfactory, which is attested to by a fairly high value of the reduced chi-square value, $\chi^2_\nu = 2.0$, and inability of the model profiles to reproduce the full extent of the rotational modulation of the Stokes *V* signature. Adding a non-axisymmetric quadrupolar component improves the fit significantly. The χ^2_ν is reduced to 1.3 and theoretical profiles achieve a reasonable description of the observations (see the solid curve in Fig. 3), even including rotational phases for which no formal detection of the polarization signatures was obtained in Section 3.1.3. In this case, the best-fitting dipolar field parameters are $B_d = 625 \pm 172$ G and $\beta_d = 12 \pm 3°$. The strength of the quadrupolar component is found to be $B_q = 214 \pm 43$ G.

The final global magnetic field geometry derived for the primary component of HD 66051 is illustrated in Fig. 4. The field structure is nearly axisymmetric and dipole-dominated. The field intensity is relatively low, with the maximum local field strength of about 700 G and the surface-averaged field modulus of 443 G.

3.3 Binary star model

We analysed the observed light curves and radial velocity variation of HD 66051 with a physical, Roche geometry model of the binary system implemented in the PHOEBE code[2] (Prša & Zwitter 2005; Prša et al. 2016). Details of our application of the PHOEBE code and the accompanying Bayesian error analysis are described in Appendix A.

Our PHOEBE analysis was performed using the four archival light curves and 14 RV measurements obtained in our study (see Table 1). The first three light curves are taken directly from N17, whereas the fourth one was obtained from the ASAS-3 *V*-filter data base (Pojmanski 2002). As discussed earlier, the photometry reveals out-of-eclipse modulation, which is thought to be produced by spots on the surface of the primary star. Non-uniform brightness distributions in Ap/Bp stars are caused by surface chemical inhomogeneities induced by strong magnetic fields. These structures are thought to be stable for at least several decades. Although PHOEBE includes a spot modelling option, it does not incorporate a physical model of the metallicity-dependent flux redistribution required for a quantitative interpretation of the photometric variations of Ap/Bp stars in different bands (e.g. Shulyak et al. 2010b; Krtička et al. 2012). For this reason, and to avoid introducing additional free (and degenerate) spot parameters, we chose to remove the spot-induced variations from all the photometric data prior to PHOEBE modelling. This was accomplished by prewhitening the photometric data with second-order Fourier functions fitted to the out-of-eclipse regions of each light curve.

PHOEBE addresses limb darkening at both the bolometric and individual filter levels. The code allows for interpolation of limb darkening coefficients, computed for model atmosphere grids according to several laws, of which we chose the square-root law. We adopted the gravity-darkening coefficients per filter from Claret & Bloemen (2011), according to the effective temperatures and

[1] http://www.astro.uu.se/~oleg/gstokes.html

[2] http://phoebe-project.org/

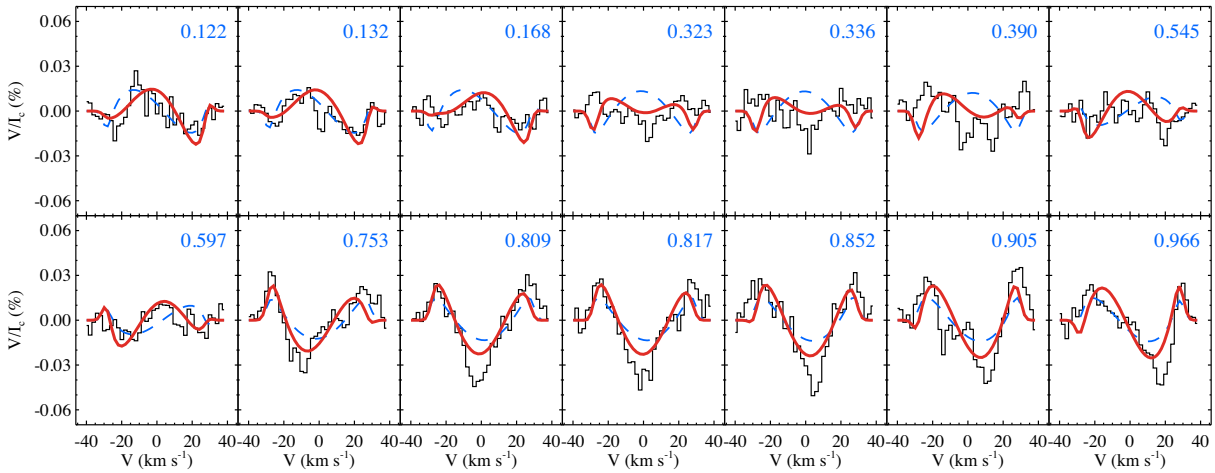

Figure 3. Comparison of the observed (black histogram) LSD Stokes *V* profiles of HD 66051 with the model profiles for the dipole (blue dashed line) and dipole+quadrupole (red solid line) magnetic field geometries discussed in the text. Rotational phases are indicated in the upper right corner of each sub-panel.

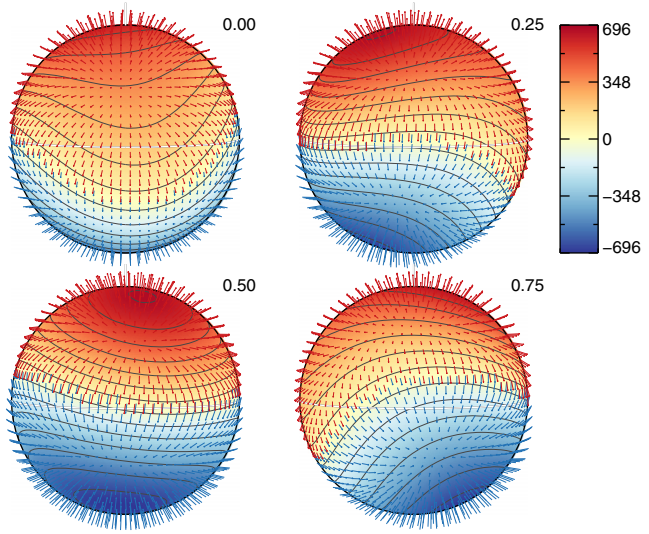

Figure 4. Magnetic field topology of the primary component of HD 66051. Distribution of the radial magnetic field component (colour plot) and the field vector orientation (red and blue vectors) are shown at four rotation phases. The field strength is given in gauss. The star is shown at the inclination angle of 86°.

surface gravities reported by N17. We did not include any third light and calculate un-binned models. The prior parameter distributions employed for the Markov Chain Monte Carlo analysis described in Appendix A are indicated in Table 2. Uniform priors in the specified ranges were adopted for all parameters except $T_{\rm eff}$, for which we used Gaussian priors according to the N17 results. (Our own spectroscopic analysis presented below largely confirms these temperatures.) The second-order Fourier term removed to account for the photometric spot modulation also effectively removes all signal associated with the rotation of either component due to the tidal synchronization of the system. Therefore, any modulation caused by varying the albedo of either component is also removed. For this reason, we choose to fix the albedo of both components to unity.

The final PHOEBE models and residuals for each observed data set (light curves and RVs) are shown in Figs 5 and 6. The final model parameters as extracted from the posterior distributions (shown and discussed in Appendix A) are listed in Table 2. The derived fundamental stellar parameters are given in Table 3. All models show a good fit to observations with no structure to the residuals. We note that the distortions of the simulated RV curves close to phase 0.0 for the primary and phase 0.5 for the secondary seen in Fig. 6 are real. These features represent manifestation of the Rossiter–Mclaughlin effect (McLaughlin 1924; Rossiter 1924).

Table 2. Free parameters of the PHOEBE model and the corresponding priors used in the Bayesian optimization and error analysis. For each parameter we list the units, when applicable, the priors, and the best-fitting values together with the 95 per cent confidence intervals.

Parameter	Prior	Best fit
$L_B^{(1)}/L_B^{(1+2)}$ (per cent)	(50, 100 per cent)	$91.4817^{+0.0035}_{-0.0035}$
$L_V^{(1)}/L_V^{(1+2)}$ (per cent)	(50, 100 per cent)	$90.5396^{+0.0027}_{-0.0032}$
$L_{I_c}^{(1)}/L_{I_c}^{(1+2)}$ (per cent)	(50, 100 per cent)	$89.1629^{+0.0065}_{-0.0065}$
$L_{ASAS-V}^{(1)}/L_{ASAS-V}^{(1+2)}$ (per cent)	(50, 100 per cent)	$90.7^{+2.1}_{-2.8}$
i (°)	(75, 90)	$86.141^{+0.087}_{-0.073}$
M_2/M_1	(0, 1)	$0.5549^{+0.0063}_{-0.0068}$
$a(R_\odot)$	(15, 25)	$20.203^{+0.098}_{-0.096}$
γ (km s^{-1})	(−10, 10)	$-2.14^{+0.37}_{-0.36}$
HJD$_0$ (d)	(2452167.87 ± 0.2)	$2452167.8724^{+0.0017}_{-0.0017}$
$P_{\rm orb}$ (d)	(4.7, 4.8)	$4.7492148^{+0.0000015}_{-0.0000015}$
$T_{\rm eff}^{(1)}$ (K)	(12500, 500)	12100^{+1000}_{-900}
Ω_1	(4, 15)	$7.831^{+0.048}_{-0.047}$
$T_{\rm eff}^{(2)}$ (K)	(8000, 500)	8100^{+900}_{-700}
Ω_2	(4, 15)	$9.29^{+0.11}_{-0.11}$

3.4 Atmospheric parameters and abundances

3.4.1 Luminosity ratio and hydrogen line profiles

We determined atmospheric parameters of the HD 66051 components taking advantage of their accurately determined masses, radii, and relative luminosities. According to the results of the previous section, fundamental surface gravities are log $g_1 = 4.05$ and log

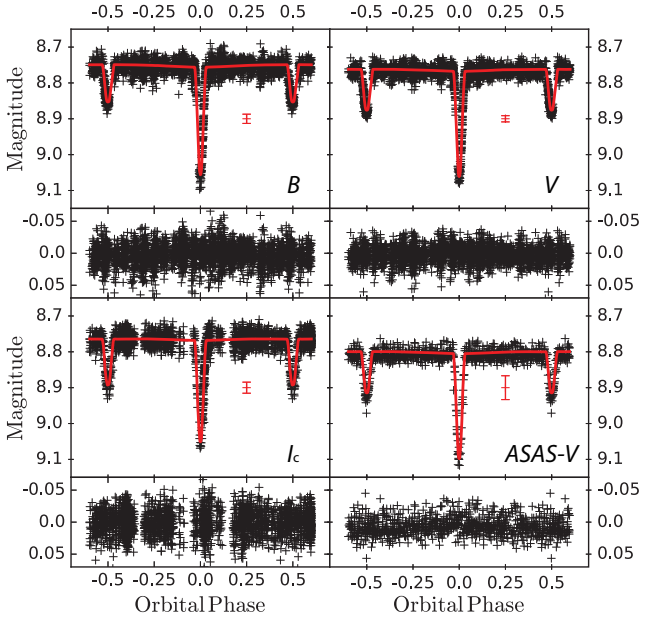

Figure 5. Comparison of the photometric measurements of HD 66051 in different bands (black crosses) with the PHOEBE light curve models (red solid curves) corresponding to the median parameter values reported in Table 2. The panels show Johnson B (*upper left*), V (*upper right*), and Cousins I_c (*lower left*) with observations from N17 and Johnson V (*lower right*) with data from the ASAS-3 data base (Pojmanski 2002). The average error bar is shown in red. Residuals are displayed below each light curve.

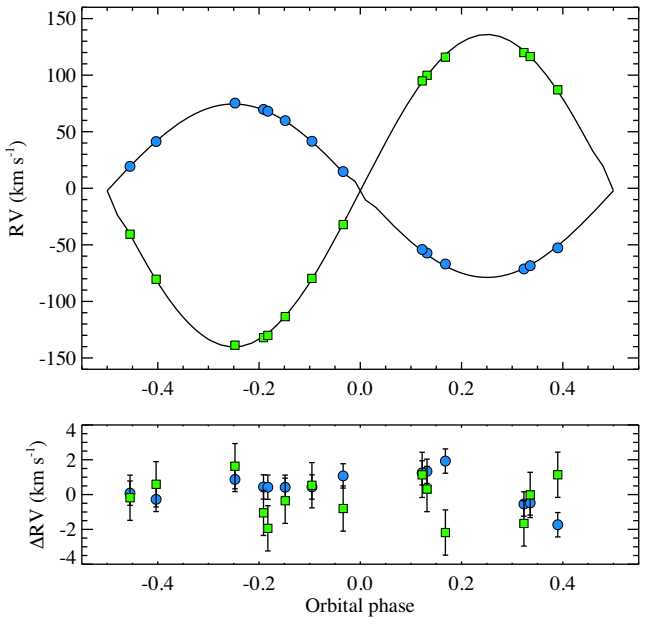

Figure 6. Comparison of the radial velocity measurements for the primary (blue circles) and secondary (green squares) component of HD 66051 with the PHOEBE model radial velocity curves (solid lines). The bottom panel shows residuals after subtracting the best-fitting model from the data.

$g_2 = 4.40$ for the primary and secondary, respectively. Keeping these $\log g$ values fixed, we calculated a grid of LLMODELS (Shulyak et al. 2004) atmospheric models using abundances of HD 66051 A reported by N17 and assuming the solar photospheric chemical composition (Asplund et al. 2009) for the secondary. The effective temperatures were varied within a 12000–13500 K interval for the primary and a 8000–9500 K range for the secondary, respectively. The theoretical spectral energy distributions of both components were convolved with the response curves of the Johnson B, V, and Cousins I_c filters (Mann & von Braun 2015) and compared to the observed luminosity ratios in these three bands using $R_1/R_2 = 2.781/1.390 = 2.000$. This analysis allowed us to establish that the effective temperature of the secondary star given by $T_{\rm eff}^{(2)} = 3507 + 0.419 \times T_{\rm eff}^{(1)}$ provides a consistency with the observed luminosity ratios over the entire considered range of $T_{\rm eff}^{(1)}$.

Table 3. Derived physical parameters for the primary and secondary components.

Parameter	Primary	Secondary
M ($M_\odot$)	$3.155^{+0.060}_{-0.057}$	$1.751^{+0.038}_{-0.039}$
R ($R_\odot$)	$2.781^{+0.034}_{-0.034}$	$1.390^{+0.042}_{-0.042}$
$\log g$ (dex)	$4.049^{+0.011}_{-0.010}$	$4.395^{+0.021}_{-0.021}$

We then refined the effective temperatures using the observed composite hydrogen line profiles. Theoretical spectra around the hydrogen Balmer lines were calculated with the SYNTH3 code (Kochukhov 2007) for both components. These calculations were then combined using appropriate radial velocity shifts, continuum fluxes (also calculated with SYNTH3), and the observed ratio of radii. The resulting composite synthetic spectra around the Hα, Hβ, and Hγ lines were compared with the observed spectra at phases 0.323 and 0.753. These observations were chosen because they correspond to the largest velocity separation between the components and hence exhibit the most clear asymmetry of the hydrogen line shapes due to contribution of the secondary.

We found that, taking into account the previous constraint on the relative $T_{\rm eff}$ values, a good agreement with observations (see Fig. 7) is achieved for $T_{\rm eff}^{(1)} =$ 12700–13300 K and $T_{\rm eff}^{(2)} =$ 8800–9100 K. We therefore adopted $T_{\rm eff}^{(1)} = 13000 \pm 300$ K and $T_{\rm eff}^{(2)} = 9000 \pm 150$ K for the subsequent analysis. This determination of the effective temperature of the primary is broadly consistent with the 12050–12750 K range obtained by N17 by applying different photometric calibrations to the unresolved Strömgren and Geneva photometric measurements of HD 66051. On the other hand, our $T_{\rm eff}^{(2)} = 9000$ K is higher than $T_{\rm eff}^{(2)} \sim 8000$ K suggested by these authors.

3.4.2 *Spectral disentangling*

We performed a binary spectral disentangling (separation), using the entire collection of our 14 ESPaDOnS spectra of HD 66051. These calculations were carried out for several dozen 100–200 Å wide wavelength regions in the interval between 3940 and 7870 Å with the help of the disentangling method described by Folsom et al. (2010, 2013b). The radial velocities of both components were fixed to the values measured from LSD profiles (Section 3.1.2). The average spectra of HD 66051 A and B were derived iteratively, using an IDL implementation of the truncated Newton optimization algorithm. Continuum normalization of short segments of individual observations was refined simultaneously with the derivation of the component spectra, using quadratic or cubic polynomials.

An application of this disentangling procedure is illustrated in Fig. 8 for the 4475–4505 Å region. This figure shows individual observed spectra, the final fit obtained by the disentangling code, and the resulting mean, separated spectra of the primary and secondary.

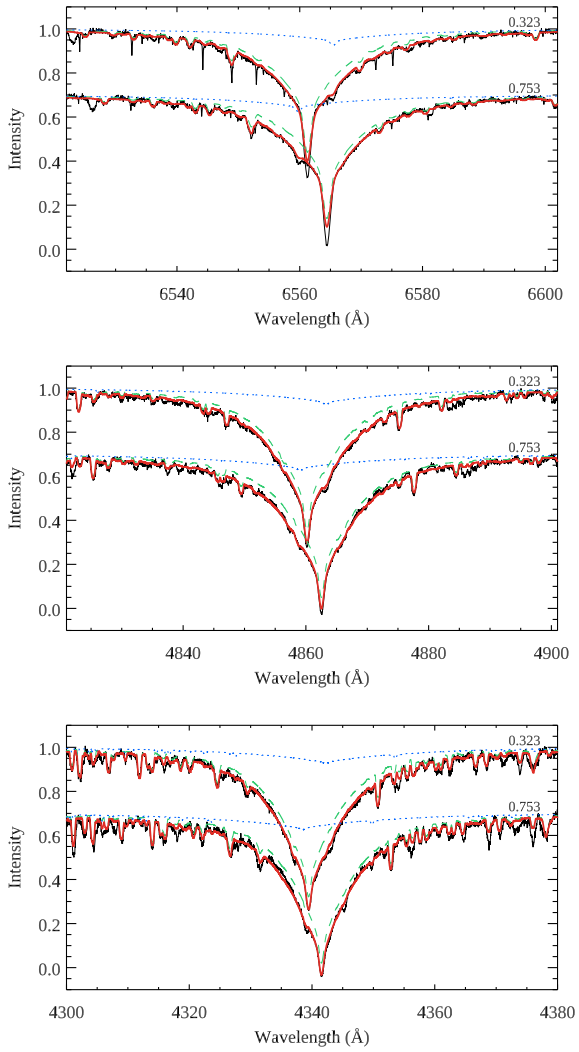

Figure 7. The observed profiles of the Hα, Hβ, and Hγ hydrogen Balmer lines (thin solid black line) at the phases of maximum relative velocity shift between the binary components compared to the composite synthetic spectra (thick solid red line) computed for $T_{\rm eff}^{(1)} =$ 13000 K and $T_{\rm eff}^{(2)} =$ 9000 K. The contributions of the primary and the secondary are shown with the green dashed and blue dotted lines, respectively. The profiles for phase 0.753 are offset vertically by −0.15.

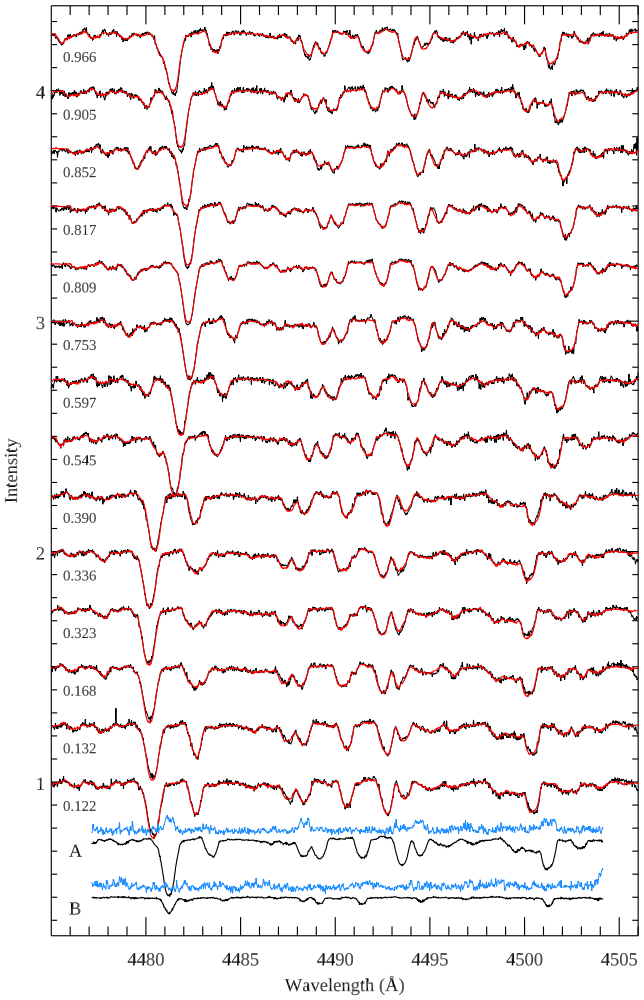

Figure 8. Illustration of the spectral disentangling procedure in the 4475–4505 Å wavelength region. The observed spectra are shown with the thin black lines. The thick red lines correspond to the binary model spectra. The profiles are offset vertically and arranged according to the orbital phase indicated to the left. The final disentangled spectra (thick black curves) are shown at the bottom of the plot together with the shifted and scaled standard deviation profiles (light blue curves).

As a by-product of this analysis, we also calculated the standard deviation spectra characterizing residuals of the fit in the rest frames of the primary and the secondary. This information will be used below (Section 3.5) for the search of intrinsic line profile variability.

The resulting high-quality (S/N ratio of about 500) mean spectrum of the primary component was compared to a theoretical synthetic spectrum for the purpose of obtaining an accurate estimate of the projected rotational velocity, $v_{\rm e} \sin i$, and verifying the element abundances reported by N17. The synthetic spectrum of HD 66051 A was computed with the SYNTH3 code for the $T_{\rm eff} =$ 13000 K, $\log g = 4.05$ atmospheric model, zero microturbulent velocity and adopting a line list retrieved from the VALD data base. The continuum dilution by the secondary was taken into account by combining the synthetic spectrum of the primary with a featureless continuum flux spectrum of the secondary using the BINMAG IDL code.[3] This software was then employed for analysis of individual wavelength regions and for an interactive adjustment of stellar parameters, including abundances and $v_{\rm e} \sin i$.

The projected rotational velocity of the primary, $v_{\rm e} \sin i = 30.5 \pm 1.1$ km s^{-1}, was inferred by fitting about 30 unblended spectral lines. The derived value is consistent with 29.6 ± 0.4 km s^{-1} expected from the oblique rotator relation assuming synchronization and alignment of the rotational and orbital axes.

We assess whether our spectra are compatible with the abundance pattern presented by N17. We do not carry out a complete new abundance analysis since, at this stage, our central aim is to scrutinize the evidence that the abundance pattern of the primary resembles that of an HgMn-type star. As commonly practiced by spectroscopic studies of these stars (Woolf & Lambert 1999; Monier, Gebran & Royer 2015; Monier et al. 2018), identification of the absorption lines and measurement of large overabundances of certain key elements, such as Xe, Ga, Mn, Au, Pt, Hg, is necessary for assigning the HgMn peculiarity type. However, a conclusive identification and reliable abundance measurement of some of these elements

[3] http://www.astro.uu.se/~oleg/binmag.html

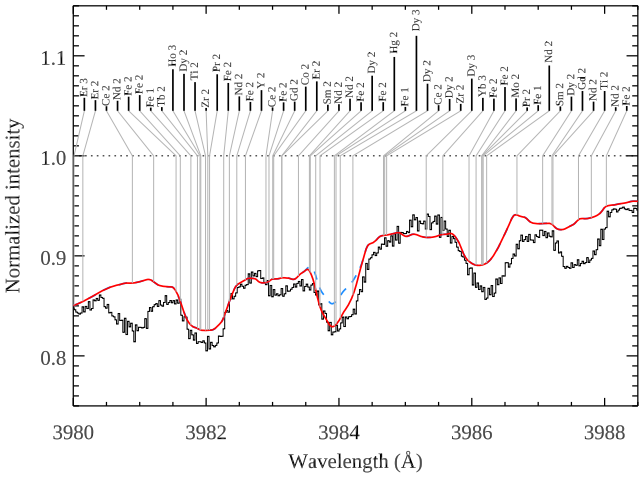

Figure 9. Disentangled spectrum of the primary component of HD 66051 (black histogram) in the vicinity of the Hg II 3984 Å line compared to the synthetic spectrum calculated with the abundances from N17 (red solid line) and with solar abundance of Hg (blue dashed line). The vertical lines indicate positions of the main spectral features contributing to this wavelength region. The length of the bar below the ion identification indicates the relative line strength.

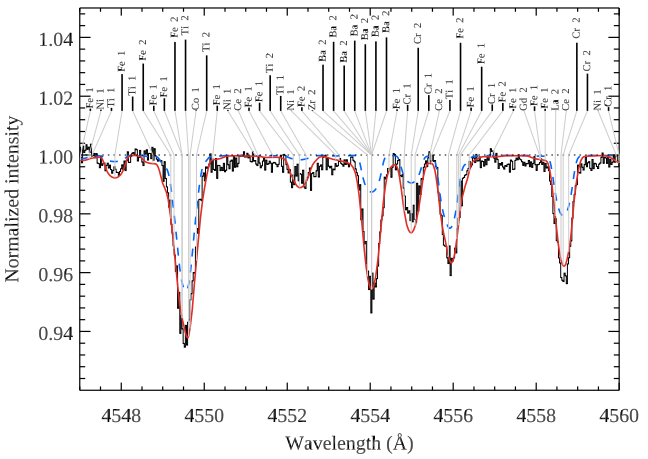

Figure 10. Disentangled spectrum of the secondary component of HD 66051 (black histogram) compared to the synthetic spectrum calculated with the enhanced Fe-peak and Ba abundances (red solid line) and with solar element abundances (blue dashed line). The vertical lines indicate positions of the main spectral features contributing to this wavelengths region. The length of the bar below the ion identification indicates the relative line strength.

may be challenging for HD 66051 A, given its relatively rapid rotation and the presence of numerous unidentified rare-earth blends. To this end, we have visually compared our disentangled spectrum of HD 66051 A with the synthetic spectrum calculated using the abundances reported by N17.

This assessment leads to mixed results. The previous abundance estimates of common Fe-peak (Fe, Ti, Cr, Mn), light (Mg, Ca, Si), and rare-earth (Eu, Nd, Pr, Dy, Ho) elements exhibiting many (or a few well-known) strong lines appear to be accurate. The absence of the He I 5876 Å line suggests that helium is more underabundant ([He] ≤ -2.2) than determined by N17. At the same time, large overabundances of many other elements estimated based on a small number of weak spectral features are questionable. For some elements (Ga, Au, Hg), a handful of lines predicted to be observable in the spectrum of the primary appear to be minor contributors to blends with known lines of other elements and/or overlap with broad unidentified features in the observed spectrum likely produced by rare-earth elements. For other elements (Cl, P, S, Xe, Lu, Hf, Pt, Pb), our spectrum synthesis based on published abundances produces unobserved spectral details, suggesting that the reported concentrations of these elements are overestimated by at least 0.5–1.5 dex. Moreover, in many cases no satisfactory fit to observations could be achieved even after implementing abundance reductions in the spectrum synthesis, suggesting the influence of unrecognized blends.

The ambiguous identification of the Hg II 3984 Å line, illustrated in Fig. 9, is symptomatic of the problems described above. On the one hand, our spectrum synthesis with the reported 3.7 dex mercury overabundance does not contradict the disentangled spectrum of the primary in the vicinity of this Hg II line. On the other hand, a closer inspection of the synthetic spectrum reveals that the mercury line is a weaker component of the blend with the Dy III 3984.02 Å feature. In this situation, a determination of the Hg abundance hinges on the knowledge of the doubly ionized Dy spectrum. Moreover, one can also see major discrepancies between the observed and theoretical spectra in the form of broad, unidentified lines at 3981 and 3987 Å, likely stemming from incomplete and inaccurate rare-earth line lists in this spectral region. In the presence of such artefacts, we do not believe that the reality of the Hg absorption can be ascertained with confidence. No other optical Hg I or II spectral lines are predicted to be deeper than 2–3 per cent of the continuum (before Doppler and instrumental broadening) by our calculations.

We carried out similar comparison of the disentangled observations with the synthetic spectra of the secondary, corrected for the continuum dilution by the primary. In this analysis we made use of the $T_{\rm eff} = 9000$ K, $\log g = 4.40$ model atmosphere and adopted a microturbulent velocity of 2 km s^{-1}. It turns out that our initial assumption of the solar abundance table provides a poor description of the spectrum of the secondary. Based on the analysis of about one hundred spectral features in the 4000–6200 Å wavelength interval, we found that observations are best matched with a moderate enhancement or near-solar abundances of light elements ([O] = +0.25, [Ca] = 0.0, [Si] = +0.3, [Mg] = +0.3), a prominent underabundance of carbon and scandium ([C] ≤ -0.5, [Sc] $= -0.6$), significant overabundance of the Fe-peak elements ([Ti] = +1.0, [Cr] = +1.2, [Fe] = +0.9), and a large enhancement of heavy elements ([Y] = +1.6, [Sr] = 1.7, [Ba] = +2.7). Fig. 10 illustrates the comparison of the calculations and disentangled spectrum of the secondary for the region around the Ba II 4554 Å transition. Large overabundances of Fe, Cr, and Ba are readily apparent.

The abundance characteristics of the secondary uncovered by our analysis, in particular a deficiency of Sc combined with an overabundance of Fe-peak and heavy elements, suggests that HD 66051 B is a fairly extreme metallic line (Am) star.

The projected rotational velocity of the secondary was found to be 19.1 $\pm$ 0.9 km s^{-1}, which is higher than $v_{\rm e} \sin i = 14.8 \pm 0.5$ km s^{-1} expected for the synchronized rotation.

3.5 Line profile variability

As was mentioned in Section 3.4, we have investigated intrinsic profile variability of individual spectral lines as part of the binary disentangling procedure. To this end, a correlation of an enhancement of the residuals with line positions in the spectrum of one or both of the binary components points to intrinsic (rotational) spec-

tral variability of that star. As an example of this situation, Fig. 8 shows peaks in the standard deviation spectrum coinciding with the Mg II 4481 Å triplet, Ti II 4488.3, and Ho III 4494.5 Å lines, and a blend at $\lambda \approx 4501$ Å comprising one Nd III and several Ti II lines contributed by the primary component of HD 66051. Using similar analysis across the entire available wavelength range, we were able to establish persistent variability of all Ti II lines and weaker changes in the absorption features of O I, Si II, Mg II, Nd II, Pr II, Eu II, and Ho III for the primary star. No evidence of intrinsic variability was found for any lines of the secondary component.

To obtain further information on these line profile changes, we compared the LSD Stokes *I* spectra constructed using the full line mask, as discussed in Section 3.1.1, with the LSD profiles obtained for the masks containing only Fe (1056 lines), Ti (99 lines), and Si (74 lines) absorption features. For the latter three calculations we made use of the multiprofile capability of the LSD code described by Kochukhov et al. (2010) to recover clean mean profiles of a given element, with contributions by all remaining lines taken into account via an independently derived second LSD profile. The resulting LSD profiles are shown in Fig. 11 for all observations except phases 0.545 and 0.966 for which the line of the primary star is partially blended by the contribution of the secondary. As evident from this figure, a very similar weak variability pattern is present in the LSD profiles obtained with all metal lines and with Fe lines alone. This is not surprising considering that Fe lines dominate the metal line mask. In comparison, the Si LSD profiles exhibit changes of similar magnitude but with a different phase dependence. The strongest spectral changes are seen for the Ti LSD profiles. In this case, the variability pattern is somewhat reminiscent of that of Fe but is more distinct.

To quantify the spectral variability of HD 66051 A, we studied the equivalent width and centre-of-gravity radial velocities extracted from the set of LSD profiles displayed in Fig. 11. These measurements are illustrated in Fig. 12. For the strongest variability case (Ti lines), the radial velocity varies by 5.0 km s^{-1} (peak-to-peak) and the equivalent width changes by 30 per cent. For Fe and Si, the variability amplitudes are ≈ 3 km s^{-1} and 15–20 per cent for the radial velocity and equivalent width, respectively. For all three elements considered here both the centre-of-gravity radial velocity and the equivalent width exhibit a coherent variation when phased with $P_{\rm orb} = 4.749215$ d, confirming that the axial rotation of HD 66051 A is indeed synchronized with its binary orbital motion.

4 CONCLUSIONS AND DISCUSSION

In this study we carried out a detailed analysis of the unique early-type eclipsing binary system HD 66051. This object was identified by previous photometric studies as an unusual example of a star showing both detached binary eclipses and a smooth out-of-eclipse photometric modulation typical of α^2 CVn-type variables. Our high-resolution, time series spectropolarimetric observations of HD 66051 demonstrated the presence of a global, predominantly dipolar magnetic field on the surface of the primary component. No evidence of a magnetic field was found for the secondary. The spectral lines of the primary exhibit variability (in addition to the Doppler shifts due to the orbital motion), in terms of both the equivalent width and line shapes, which is different depending on the considered chemical element. The strongest variability is found for the ionized Ti lines.

These magnetic and spectral variability characteristics suggest that HD 66051 A is a magnetic chemically peculiar star with a non-uniform surface distribution of chemical abundances. The chemical spots in such stars are known to produce a flux redistribution between different parts of their spectra, resulting in an inhomogeneous surface brightness distribution at any given wavelength (e.g. Krtička et al. 2012). The rotation of the primary is synchronized with the orbital motion, giving rise to a stable photometric variability superimposed on to the eclipses.

The previous detailed spectroscopic study of HD 66051 by N17 provided abundance estimates for 46 chemical elements, including many exotic light and heavy species typically identified in the spectra of slowly rotating HgMn stars. Their abundance analysis relied on a single observation of the composite binary spectrum aided by an additional lower-quality spectrum taken during the secondary eclipse. Based on their abundance analysis results and comparison with the surface chemistry of the extreme HgMn star HD 65949 (Cowley et al. 2010), N17 concluded that the primary is an HgMn-related object and that the secondary is likely to be a normal star with solar abundances.

It should be noted that precision and reliability of a stellar abundance analysis quickly diminish with increasing projected rotational velocity of the star, especially in the presence of a rich and poorly understood rare-earth absorption spectrum. For this reason, typical abundance determinations for rapidly rotating Ap/Bp and HgMn stars (e.g. Glagolevskii, Ryabchikova & Chountonov 2005; Semenko et al. 2008; Fossati et al. 2011; Bailey & Landstreet 2015) are usually restricted to much fewer chemical elements than can be measured for slowly rotating stars of these types (e.g. Cowley et al. 2010; Shulyak et al. 2010a; Castelli et al. 2017). The large number of chemical elements reported by N17 for HD 66051 A deviates significantly from this trend. Their paper provides no details (such as an in-depth discussion of the abundance determination methodology or a list of spectral lines used for abundance measurements) of how the authors have tackled the formidable problem of abundance analysis of this rapidly rotating, rare-earth rich chemically peculiar star.

In the context of this study, we have acquired 14 individual epochs of spectroscopic observations of HD 66051. These data were processed with a binary disentangling algorithm, yielding high-quality, separated mean spectra of the primary and the secondary. Our spectrum synthesis analysis of the disentangled spectrum of the primary component indicates that reliable line identification is significantly hindered by the rotational broadening and blending by rare-earth lines. Our data are compatible with some of the abundance estimates (e.g. Si, Ca, Fe-peak, and rare-earth elements) made by N17. At the same time, we are not able to confirm and, in some cases, we rule out large overabundances claimed for many other elements, including those (Hg, Au, Pt, Xe, Ga) that were used by N17 to classify HD 66051 A as an HgMn-related star.

N17 suggested that the abundance pattern of HD 66051 A is similar to that of the extreme HgMn star HD 65949. However, a direct comparison of the broadened spectrum of HD 65949 from the study of Makaganiuk et al. (2011a) with the disentangled spectrum of HD 66051 A shows little resemblance (Fig. 13). Despite similar temperatures, the latter star exhibits many more and stronger metal absorption features. On the other hand, He lines are weaker in HD 66051 A, indicating an extreme helium deficiency atypical of HgMn stars. In addition, the 1 dex silicon and 4–5 dex rare-earth overabundances are also uncharacteristic of HgMn stars (Ghazaryan & Alecian 2016). To this end, the spectrum of the primary component of HD 66051 appears to be that of a typical silicon and rare-earth rich, magnetic, late-B (Bp) star, in line with its classification by Bidelman & MacConnell (1973) and Houk & Smith-Moore (1988). As illustrated by Fig. 13, this conclusion is supported by

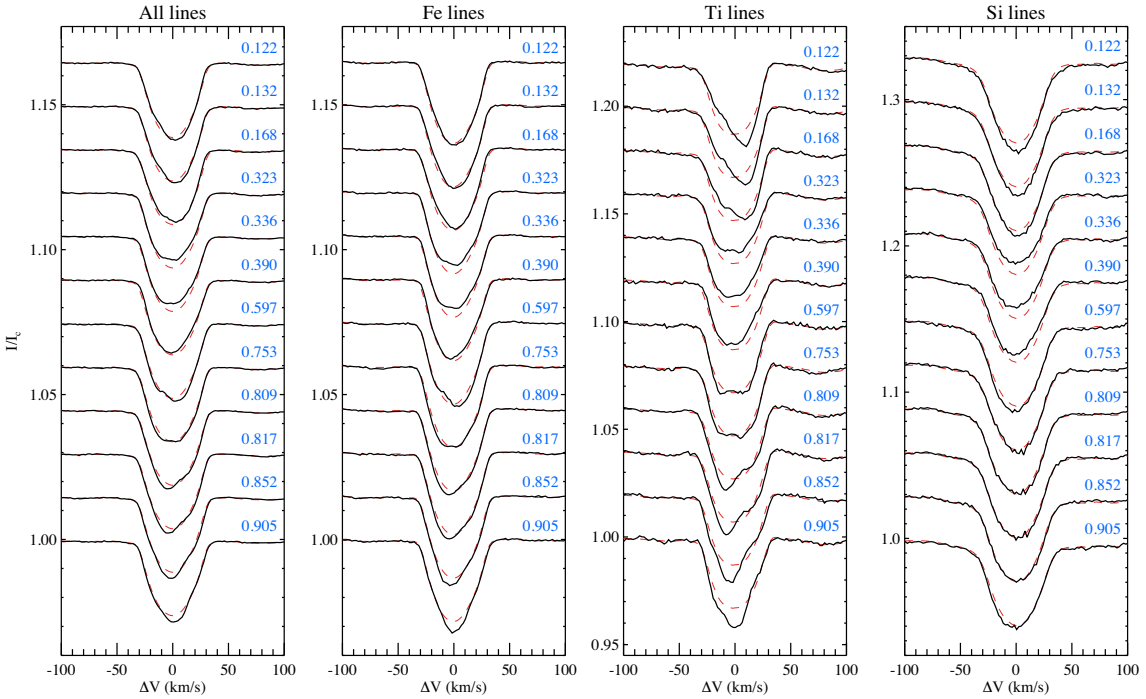

Figure 11. Variation of the LSD profiles of HD 66051 A derived from the entire set of metal lines as well as from the Fe, Ti, and Si lines. The spectra are offset vertically according to the rotational phase. The time-dependent spectra (black solid curves) are plotted together with the mean profiles (red-dashed curves).

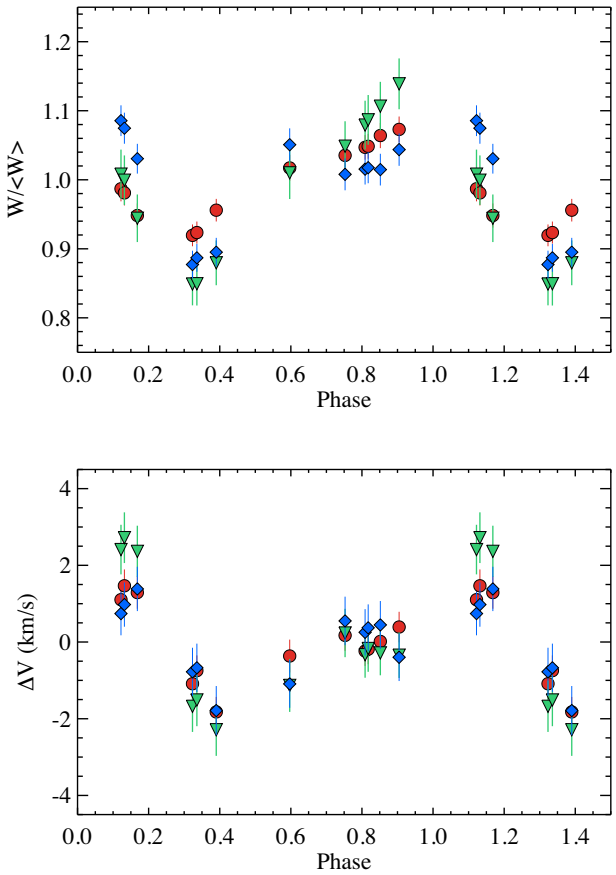

Figure 12. Variation of the relative equivalent widths (upper panel) and radial velocities (lower panel) of the Stokes *I* LSD profiles as a function of rotational phase. The symbols show measurements for Fe (red circles), Ti (green triangles), and Si (blue diamonds).

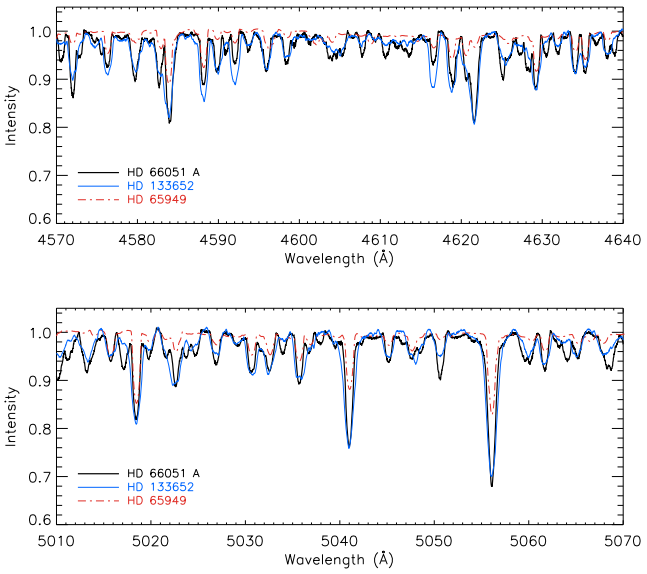

Figure 13. Comparison of the disentangled spectrum of HD 66051 A (thick solid black line) with the average spectrum of the magnetic Bp star HD 133652 (thin solid blue line) and the broadened spectrum of the extreme HgMn star HD 65949 (dashed-dotted red line).

the similarity of the line absorption in our disentangled spectrum of HD 66051 A with the spectrum of unremarkable magnetic Bp star HD 133652 (Bailey & Landstreet 2015).

Our definite detection of a global magnetic field in HD 66051 A also clearly sets this object aside from HgMn stars. The latter are thought to be non-magnetic (Shorlin et al. 2002; Aurière et al. 2010; Makaganiuk et al. 2011a, 2012; Kochukhov et al. 2011, 2013) at the 10–100 G level. Occasional claims of statistically significant

longitudinal field detections for HgMn stars can be found in the literature (Hubrig et al. 2006, 2010, 2012), but those have not been confirmed by independent follow-up studies, including re-analyses of the same observational data (Bagnulo et al. 2012; Kochukhov et al. 2013), and were never supported by direct Zeeman polarization signature detections such as that presented here for HD 66051 A.

The high S/N ratio disentangled spectrum of the faint secondary enabled a new insight into its nature. The projected rotational velocity of the secondary suggests that its rotational period is shorter than the orbital period of the system or that its rotational axis is misaligned with the orbital axis. The spectrum of the secondary shows enhanced lines of Fe-peak elements, a deficiency of Sc and large overabundances of Sr, Y, and Ba. These abundance characteristics, as well as the lack of global magnetic field and line profile variability, are typical of metallic-line (Am) stars. This establishes HD 66051 as belonging to the group of several confirmed systems hosting both an Ap/Bp and Am components. The three other binaries in this group are HD 98088, HD 5550, and BD-19 5044L (Folsom et al. 2013b; Alecian et al. 2016; Landstreet et al. 2017). Together with HD 66051, these systems represent all well-studied close SB2s with lower-mass ($M \leq 4M_{\odot}$) magnetic Ap/Bp primaries.

We used archival broad-band photometric observations of HD 66051 together with the radial velocities derived from our data to perform binary system modelling with the PHOEBE code. This analysis provided precise fundamental radii and masses of both components. In addition, information on the wavelength-dependent luminosity ratio combined with the results of hydrogen line profile modelling allowed us to infer effective temperatures of both stars.

Our binary modelling results can be compared with the parameters of the system recently published by Paunzen et al. (2018). These authors used an earlier version of the PHOEBE code for the analysis of the same photometric light curves as investigated here. On the other hand, they relied on an independent set of (unpublished) radial velocity estimates derived from heterogeneous spectroscopic observations, including measurements from medium-resolution ($R \sim 12000$) spectra. This RV data set has phase gaps of up to about 1/3 of the orbital cycle. In comparison, the largest phase gap in our spectral time series is 0.156. Furthermore, Paunzen et al. (2018) treated their RV measurements with a separate analysis, from which they derived the mass ratio and then fixed it in the PHOEBE solution. Their study also lacked the rigorous Bayesian MCMC error assessment comparable to that presented in our paper. Likely owing to these differences, the stellar radii ($R_1 = 2.58 \pm 0.13R_{\odot}$ and $R_2 = 1.61 \pm 0.10R_{\odot}$) obtained by Paunzen et al. (2018) are marginally (at a 1.5–2.0σ level) different and less precise compared to our results. Their inclination angle ($i = 84.7 \pm 0.1^{\circ}$) is significantly lower than our estimate. On the other hand, their mass ratio ($M_2/M_1 = 0.56 \pm 0.03$) and individual component masses ($M_1 = 3.23 \pm 0.22M_{\odot}$ and $M_2 = 1.81 \pm 0.13M_{\odot}$) agree with our results within error bars.

The set of observational constraints available for HD 66051 is unprecedented for early-type stars with such extreme surface chemical abundance anomalies and magnetic field. These results open unique possibilities for detailed stellar interior structure and evolution studies. For example, one could exploit HD 66051 to test stellar structure models with radiatively driven chemical stratification (Vick et al. 2010) and put firm limits on the radius modification due to interior non-force-free magnetic fields (Valyavin, Kochukhov & Piskunov 2004). One could also probe other poorly understood interior structure processes such as mixing in the radiative zone, convective core overshoot, etc.

Our study of the HD 66051 system also offers a valuable new insight into the long-standing problem of the interplay between fossil magnetism and binarity. This object belongs to an exclusive group of about 10 well-characterized close ($P_{\rm orb} < 20$ d) SB2 systems with an early-type magnetic component (Landstreet et al. 2017; Shultz et al. 2018). Two less well-studied close SB1 binaries, HD 25267 and HD 25823, with an early-type magnetic component are also known (Mathys 2017). Seven of these SB1 and SB2 systems, including HD 66051, have $P_{\rm orb} < 10$ d. Their existence defies the well-established general trend of a lack of intermediate-mass and massive magnetic stars in close binaries and challenges theories purporting to explain this trend (Commerçon et al. 2011; Schneider et al. 2016). Evidently, these theories need to account for the formation of at least a few close systems with early-type magnetic components. Among these key objects, HD 66051 is the only known eclipsing binary and hence the only system with fundamental constraints on the component parameters and their dynamical interaction.

ACKNOWLEDGEMENTS

OK acknowledges financial support from the Knut and Alice Wallenberg Foundation, the Swedish Research Council, and the Swedish National Space Board. Part of the research leading to these results has received funding from the European Research Council (ERC) under the European Union's Horizon 2020 research and innovation programme (grant agreement N°670519: MAMSIE). The computational resources and services used in this work were in part provided by the VSC (Flemish Supercomputer Center), funded by the Research Foundation – Flanders (FWO) and the Flemish Government – department EWI. GAW acknowledges Discovery Grant support from the Natural Sciences and Engineering Research Council (NSERC) of Canada. This study is based on observations obtained at the Canada-France-Hawaii Telescope (CFHT), which is operated by the National Research Council of Canada, the Institut National des Sciences de l'Univers of the Centre National de la Recherche Scientifique of France, and the University of Hawaii.

REFERENCES

Achilleos N., Wickramasinghe D. T., 1989, ApJ, 346, 444
Adelman S. J., Gulliver A. F., Kochukhov O. P., Ryabchikova T. A., 2002, ApJ, 575, 449
Alecian E. et al., 2008, MNRAS, 385, 391
Alecian E. et al., 2015, in Meynet G., Georgy C., Groh J., Stee P., eds, Proc. IAU Symp. Vol. 307, New Windows on Massive Stars. Cambridge Univ. Press, Cambridge, p. 330
Alecian E., Tkachenko A., Neiner C., Folsom C. P., Leroy B., 2016, A&A, 589, A47
Asplund M., Grevesse N., Sauval A. J., Scott P., 2009, ARA&A, 47, 481
Aurière M. et al., 2010, A&A, 523, A40
Bagnulo S., Landi degl'Innocenti M., Landi degl'Innocenti E., 1996, A&A, 308, 115
Bagnulo S., Landolfi M., Landstreet J. D., Landi Degl'Innocenti E., Fossati L., Sterzik M., 2009, PASP, 121, 993
Bagnulo S., Landstreet J. D., Fossati L., Kochukhov O., 2012, A&A, 538, A129
Bailey J. D., Landstreet J. D., 2015, A&A, 580, A81
Bidelman W. P., MacConnell D. J., 1973, AJ, 78, 687
Braithwaite J., Spruit H. C., 2004, Nature, 431, 819
Carrier F., North P., Udry S., Babel J., 2002, A&A, 394, 151
Castelli F., Cowley C. R., Ayres T. R., Catanzaro G., Leone F., 2017, A&A, 601, A119
Claret A., Bloemen S., 2011, A&A, 529, A75

Commerçon B., Hennebelle P., Henning T., 2011, ApJ, 742, L9
Cowley C. R., Hubrig S., Palmeri P., Quinet P., Biémont É., Wahlgren G. M., Schütz O., González J. F., 2010, MNRAS, 405, 1271
Donati J.-F., Semel M., Rees D. E., 1992, A&A, 265, 669
Donati J.-F., Semel M., Carter B. D., Rees D. E., Collier Cameron A., 1997, MNRAS, 291, 658
Folsom C. P., Kochukhov O., Wade G. A., Silvester J., Bagnulo S., 2010, MNRAS, 407, 2383
Folsom C. P., Wade G. A., Alecian E., 2013a, EAS Publ. Ser., 64, 119
Folsom C. P., Likuski K., Wade G. A., Kochukhov O., Alecian E., Shulyak D., 2013b, MNRAS, 431, 1513
Foreman-Mackey D., Hogg D. W., Lang D., Goodman J., 2013, PASP, 125, 306
Fossati L., Folsom C. P., Bagnulo S., Grunhut J. H., Kochukhov O., Landstreet J. D., Paladini C., Wade G. A., 2011, MNRAS, 413, 1132
Gerbaldi M., Floquet M., Hauck B., 1985, A&A, 146, 341
Ghazaryan S., Alecian G., 2016, MNRAS, 460, 1912
Glagolevskii Y. V., Ryabchikova T. A., Chountonov G. A., 2005, Astron. Lett., 31, 327
Houk N., Smith-Moore M., 1988, Michigan Catalogue of Two-dimensional Spectral Types for the HD Stars. Volume 4, Declinations −26 deg to −12 deg
Hubrig S., North P., Schöller M., Mathys G., 2006, Astron. Nachrichten, 327, 289
Hubrig S. et al., 2010, MNRAS, 408, L61
Hubrig S. et al., 2012, A&A, 547, A90
Hümmerich S., Paunzen E., Bernhard K., 2016, AJ, 152, 104
Kochukhov O., 2007, in Romanyuk I. I., Kudryavtsev D. O., eds, Physics of Magnetic Stars. Special Astrophysical Observatory RAS, Niznij Arkhyz, p. 109
Kochukhov O., Piskunov N., Sachkov M., Kudryavtsev D., 2005, A&A, 439, 1093
Kochukhov O., Makaganiuk V., Piskunov N., 2010, A&A, 524, A5
Kochukhov O. et al., 2011, A&A, 534, L13
Kochukhov O. et al., 2013, A&A, 554, A61
Kochukhov O., Lüftinger T., Neiner C., Alecian E., MiMeS Collaboration, 2014, A&A, 565, A83
Kochukhov O., Silvester J., Bailey J. D., Landstreet J. D., Wade G. A., 2017, A&A, 605, A13
Korhonen H. et al., 2013, A&A, 553, A27
Krtička J., Mikulášek Z., Lüftinger T., Shulyak D., Zverko J., Žižňovský J., Sokolov N. A., 2012, A&A, 537, A14
Kurtz D. W., Martinez P., 2000, Baltic Astron., 9, 253
Landi Degl'Innocenti E., Landolfi M., eds, 2004, Astrophysics and Space Science Library, Vol. 307, Polarization in Spectral Lines. Kluwer Academic Publishers, Dordrecht
Landstreet J. D., 1988, ApJ, 326, 967
Landstreet J. D., Kochukhov O., Alecian E., Bailey J. D., Mathis S., Neiner C., Wade G. A., BINaMIcS Collaboration, 2017, A&A, 601, A129
Makaganiuk V. et al., 2011a, A&A, 525, A97
Makaganiuk V. et al., 2011b, A&A, 529, A160
Makaganiuk V. et al., 2012, A&A, 539, A142
Mann A. W., von Braun K., 2015, PASP, 127, 102
Markwardt C. B., 2009, in Bohlender D. A., Durand D., Dowler P., eds, ASP Conf. Ser. Vol. 411, Astronomical Data Analysis Software and Systems XVIII. Astron. Soc. Pac., San Francisco, p. 251
Mathys G., 2017, A&A, 601, A14
McLaughlin D. B., 1924, ApJ, 60, 22
Monier R., Gebran M., Royer F., 2015, A&A, 577, A96
Monier R., Gebran M., Royer F., Kilicoglu T., Frémat Y., 2018, ApJ, 854, 50
Morel T. et al., 2014, A&A, 561, A35
Neiner C., Mathis S., Alecian E., Emeriau C., Grunhut J., BinaMIcS and MiMeS Collaborations, 2015, in Nagendra K. N., Bagnulo S., Centeno R., Jesús Martínez González M., eds, IAU Symposium Vol. 305, Polarimetry, p. 61.
Niemczura E., Hümmerich S., Castelli F., Paunzen E., Bernhard K., Hambsch F.-J., Hełminiak K., 2017, Sci. Rep., 7, 5906 (N17)
Otero S. A., 2003, Inf. Bull. Variable Stars, 5480
Paunzen E. et al., 2018, A&A, in press (arXiv:1802.09753)
Perryman M. A. C. et al., 1997, A&A, 323, L49
Petit V., Wade G. A., 2012, MNRAS, 420, 773
Pojmanski G., 2002, Acta Astron., 52, 397
Prša A., Zwitter T., 2005, ApJ, 628, 426
Prša A. et al., 2016, ApJS, 227, 29
Renson P., Manfroid J., 2009, A&A, 498, 961
Rosén L., Kochukhov O., Alecian E., Neiner C., Morin J., Wade G. A., the BinaMIcS Collaboration, 2018, A&A, 613, A60
Rossiter R. A., 1924, ApJ, 60, 15
Ryabchikova T., Piskunov N., Kurucz R. L., Stempels H. C., Heiter U., Pakhomov Y., Barklem P. S., 2015, Phys. Scr, 90, 054005
Schneider F. R. N., Podsiadlowski P., Langer N., Castro N., Fossati L., 2016, MNRAS, 457, 2355
Schöller M., Correia S., Hubrig S., Ageorges N., 2010, A&A, 522, A85
Semenko E. A., Kudryavtsev D. O., Ryabchikova T. A., Romanyuk I. I., 2008, Astrophys. Bull., 63, 128
Shorlin S. L. S., Wade G. A., Donati J.-F., Landstreet J. D., Petit P., Sigut T. A. A., Strasser S., 2002, A&A, 392, 637
Shultz M., Wade G. A., Alecian E. BinaMIcS Collaboration 2015, MNRAS, 454, L1
Shultz M., Rivinius T., Wade G. A., Alecian E., Petit V., 2018, MNRAS, 475, 839
Shulyak D., Tsymbal V., Ryabchikova T., Stütz C., Weiss W. W., 2004, A&A, 428, 993
Shulyak D., Ryabchikova T., Kildiyarova R., Kochukhov O., 2010a, A&A, 520, A88
Shulyak D., Krtička J., Mikulášek Z., Kochukhov O., Lüftinger T., 2010b, A&A, 524, A66
Sikora J., Wade G. A., Power J., 2018, Contrib. Astron. Observatory Skalnate Pleso, 48, 87
Smith K. C., 1996, Ap&SS, 237, 77
Strassmeier K. G., Granzer T., Mallonn M., Weber M., Weingrill J., 2017, A&A, 597, A55
Valyavin G., Kochukhov O., Piskunov N., 2004, A&A, 420, 993
Vick M., Michaud G., Richer J., Richard O., 2010, A&A, 521, A62
Woolf V. M., Lambert D. L., 1999, ApJ, 520, L55

APPENDIX A: DETAILS OF PHOEBE ANALYSIS

To obtain a PHOEBE model with robustly determined errors, we employed a Bayesian Markov Chain Monte Carlo (MCMC) numerical scheme. Furthermore, to determine uncertainties accounting for the effect of known correlations between binary model parameters, we wrapped PHOEBE into the EMCEE code by Foreman-Mackey et al. (2013), which makes use of an ensemble, affine-invariant approach to sampling the parameter posterior distributions.

The MCMC optimization is based upon Bayes' Theorem:

$$p\,(\Theta|d) \propto \mathcal{L}\,(d|\Theta)\;p\,(\Theta)\,. \tag{A1}$$

Here, $p(\Theta|d)$ is the posterior distribution of the model parameters Θ, which are varied in the optimization given the observations d. The prior probability of the parameter vector $p(\Theta)$ is used to draw the parameter configurations, and is set as either uniform or Gaussian. The likelihood function $\mathcal{L}\,(\Theta|d)$ evaluates the likelihood that a given parameter configuration accurately reproduces the observations. For computational ease, we work in log-space where we write the likelihood as

$$\ln\mathcal{L} \propto -\frac{1}{2}\sum_i \left(\frac{d_i - M\,(\Theta)_i}{\sigma_i}\right)^2, \tag{A2}$$

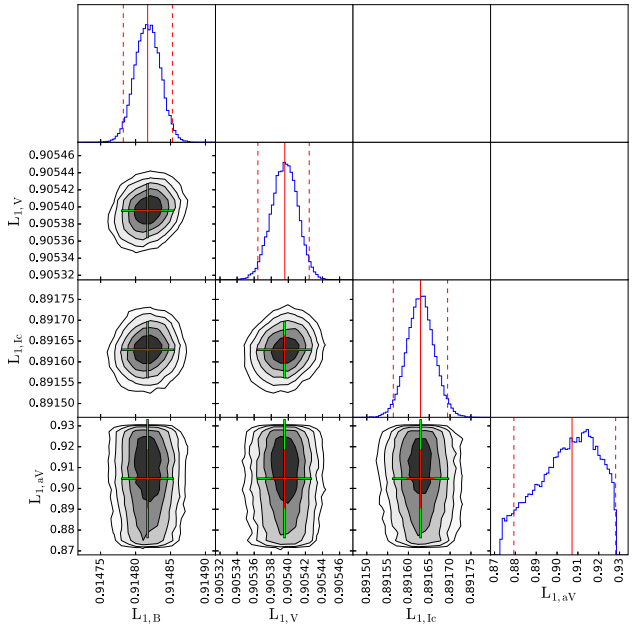

Figure A1. Marginalized posterior distributions for primary light fraction for each observed filter. Median denoted by solid vertical red line, upper and lower bounds for 95 per cent CI denoted by dashed vertical red lines.

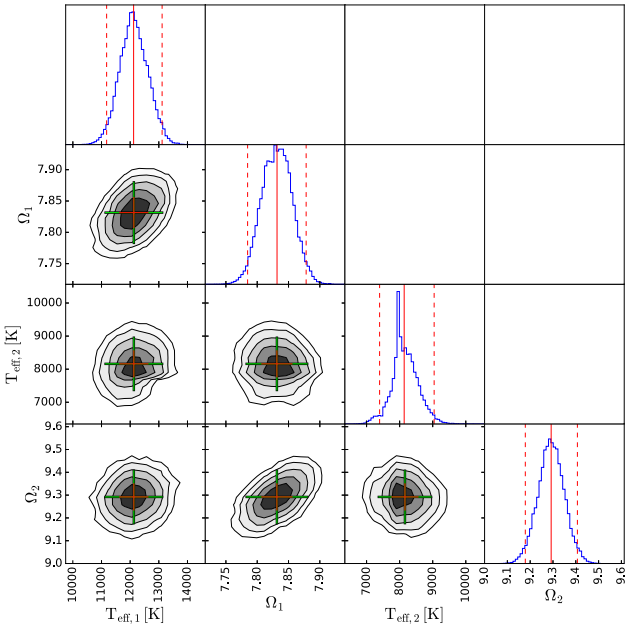

Figure A2. Marginalized posterior distributions for primary and secondary parameters. Median denoted by solid vertical red line, upper and lower bounds for 95 per cent CI denoted by dashed vertical red lines.

where σ_i represents the uncertainties on each data point d_i and $M(\Theta)_i$ is the model produced using the parameter configuration Θ.

For the MCMC analysis we used an ensemble configuration of 138 individual parameter chains and allowed the algorithm to run for 5000 iterations. After 5000 iterations, we checked the chains for convergence via auto-correlation. Once the samplings have been confirmed to have converged, we burned the first 1500 iterations and produced the posteriors for the remaining 3500 iterations. We calculated 95 per cent confidence intervals (CIs) by evaluating the Highest Posterior Density (HPD) with $\alpha = 0.05$ for all marginalized posteriors. We varied 14 parameters in total, 4 of which are passband luminosities related to scaling the model light curves to the observations, while the remaining 10 are physical parameters, all of which are listed in Table 2.

The marginalized posteriors and HPD error estimates are shown in Figs A1–A3. Fig. A1 shows the marginalized posteriors for the passband luminosities derived by PHOEBE. It is clear from these posteriors that the ASAS *V*-band curve has little impact on the likelihood as the posteriors recover the priors. This can be understood in terms of the larger formal error bars associated with these data compared to the other light curves. Figs A2 and A3 show the posteriors for individual stellar parameters and system parameters, respectively. While most posteriors are well behaved, the posteriors for the inclination, *i*, show complex structures, best described as an unresolved bimodal distribution. However, as the HPD estimation includes both nodes in the CIs, the errors are propagated properly. This is reflected in the propagated errors on the derived stellar masses in Table 3, however, it does not push the estimate of either mass more than a few percent above or below their median values. Furthermore, despite a Gaussian prior on $T_{\rm eff}^{(2)}$, the posteriors climbed to systematically higher values, and has a CI range of 1600 K.

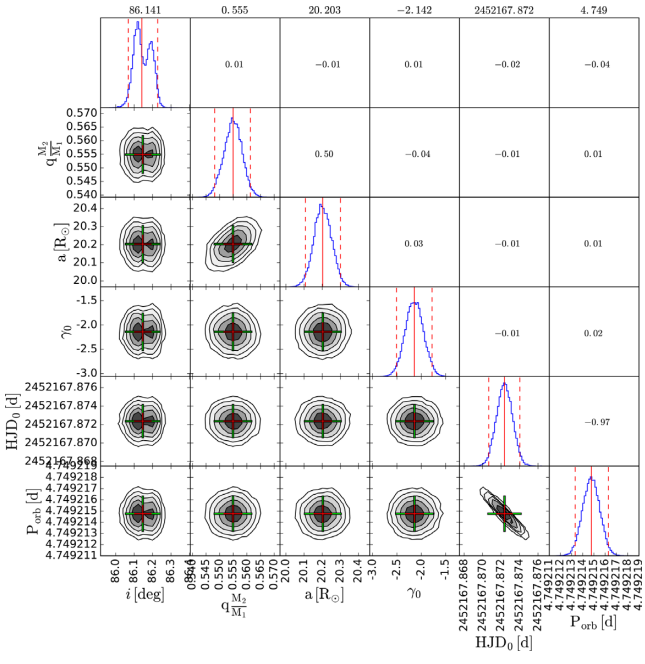

Figure A3. Marginalized posterior distributions for system parameters. Median denoted by solid vertical red line, upper and lower bounds for 95 per cent CI denoted by dashed vertical red lines.

The final light curve and radial velocity variation models presented in the paper were constructed using the median values of the parameters estimated from marginalized posteriors.

This paper has been typeset from a TEX/LATEX file prepared by the author.